Supporting Information

Beyond Metal-Centric Catalysis in Dual-Atom Catalyst: Hydrogenated Bridge NH Sites Drive Formic Acid Decomposition via Co-Cu Synergy

Jin Zhang, Xiaoli Chen, Yuxuan Wu, Fang-Fang Wang,* De-Li Chen*

[1]Key Laboratory of the Ministry of Education for Advanced Catalysis Materials, Institute of Physical Chemistry, Zhejiang Normal University, 321004 Jinhua, China

1. Theoretical details

There are several different *U* values reported in the literature. Considering that the Co site is an important adsorption site for *H adsorption, a different *U* value for Co was used to perform some calculations and make a comparison with those in the present study. The results show that the δE starting from the $H_{N1}H_{N2}/CoCuN_6$-C structure was calculated to be 1.49 eV when *U* value[S1,S2] of 4.0 was applied using the DFT+U method, close to the δE value of 1.50 eV with a *U* value of 3.3. This indicates that the calculations in the present study are able to provide reliable results.

For the calculations of reaction pathways, different spin states of both Co and Cu were considered, and the stable states were used for the intermediates. To clarify the spin states, the magnetic moments of metal atoms in several important intermediates are listed in Table S1. As shown in Table S1, for the stable $CoCuN_6$-C structure, the magnetic moments of Co and Cu atoms are 1.10 and 0.45 μ_B, respectively. Meanwhile, its higher spin state with corresponding values of 1.95 and 0.54 μ_B is thermodynamically unstable by 0.65 eV. When *H is adsorbed at the bridge N1 and N2 sites ($H_{N1}H_{N2}/CoCuN_6$-C), the magnetic moments of Co and Cu are only slightly reduced to 1.00 and 0.02 μ_B, probably due to the structural distortion. Remarkably, when *H is adsorbed at the Co site ($H_{N2}H_{Co}/CoCuN_6$-C), a low spin state of Co is obtained, with a magnetic moment of 0.03 μ_B. This indicates that a σ-bond (Co-H) is formed between the unpaired *d* electrons of the Co atom and the *s* electrons of H. Overall, a moderate spin state was found for the Co atom in the DAC, while the high spin state is thermodynamically unstable. The adsorption of H species leads to a low spin state for the Co atom. This phenomenon is also observed in CoN_4-C SAC. Therefore, for the intermediates and transition states during HCOOH dehydrogenation, the spin states of Co were found to vary from 0.00 to 1.10 μ_B.

Table S1. Spin states of catalyst models and several important intermediates

Structures	Co (μ_B)	Cu (μ_B)	E_{rel} (eV)
$CoCuN_6$-C	1.10	0.45	0.00
	1.95	0.54	0.65
	0.00	0.00	0.68
$H_{N1}H_{N2}/CoCuN_6$-C	1.00	0.02	0.00
	1.09	0.48	0.94
$H_{N2}H_{Co}/CoCuN_6$-C	0.03	0.44	0.00
	1.52	0.49	0.88
$4H/CoCuN_6$-C	0.00	0.00	0.00
	0.42	0.15	0.85
CoN_4-C	1.03	/	0.00
	2.42	/	0.55
	0.00	/	0.69
IM3	1.00	0.02	0.00
	0.00	0.00	0.25
	1.04	0.26	0.39
	1.06	0.46	0.76
TS4	0.51	0.52	0.00
	0.40	-0.53	0.01
	0.84	0.54	0.26
	0.00	0.00	0.27
	1.62	0.54	0.43
	2.44	0.52	0.80
IM6	0.96	-0.03	0.00
	0.00	0.00	0.26
	1.03	0.23	0.47
	1.12	0.50	1.61
TS7	0.86	0.00	0.00
	2.51	-0.01	0.03
	0.00	0.00	0.38
	0.96	0.20	0.42

2. Solvent effect

Decomposition of the first HCOOH in solvent

The decomposition pathways of FA were systematically re-evaluated under explicit solvation conditions to assess aqueous phase effects, as illustrated in Figure S3 (transition states in Figure

S4). For the first FA decomposition cycle, the solvated system retains nearly identical mechanistic steps and energy profiles to the vacuum-phase calculations. The initial proton transfer from FA to bridge nitrogen N1 (TS1a) proceeds via α-H abstraction with a minimal activation free energy (0.25 eV), forming the *HCOO intermediate (IM1a). Subsequent spontaneous desorption of *HCOO from the Co site occurs with negligible barrier (0.12 eV), yielding IM2a. The second dehydrogenation step, β-H transfer to adjacent nitrogen N2, exhibits a significantly higher barrier of 1.07 eV, generating the thermodynamically stable intermediate (TDI, IM3a) with a relative energy of –1.01 eV. Hydrogen evolution proceeds through two concerted steps: (1) *H1 migration from N1 to Co (TS4a, $\Delta G^{\ddagger}$ = 1.09 eV, ΔG = +0.71 eV) and (2) H–H bond formation at the Co site (TS5a, $\Delta G^{\ddagger}$ = 0.87 eV, ΔG = –0.30 eV). The overall thermodynamic span (δE = 1.58 eV) aligns closely with vacuum-phase calculations (1.61 eV, <2% deviation), confirming the negligible solvation effects on FA decomposition energetics. This mechanistic preservation highlights the dominance of intrinsic catalyst-adsorbate interactions over environmental screening effects.

Decomposition of the second HCOOH in solvent

In contrast to the first decomposition pathway, the second formic acid (FA) decomposition exhibits a reduced thermodynamic driving force, as evidenced by the diminished δE value (blue curves in Figure S3). The rate-determining intermediate (TDI) corresponds to intermediate IM6a at a relative energy of –1.25 eV, marginally higher than the –1.38 eV observed for the analogous IM6 state in vacuum. This energy shift suggests that explicit solvation via the water model weakens reactant-catalyst interactions by 0.13 eV through competitive hydrogen bonding. A rotation of the chemisorbed HCOOH molecule in IM6a leads to IM7a state, where both H1 and H2 atoms point to

the active sites. Then, H1 atom abstracts from HCOOH, forming IM8a state with a minimal energy barrier (TS6a) of 0.14 eV. Subsequent desorption of HCOO* gives rise to IM9a state along with a moderate activation energy of 0.61 eV. The following H2 desorption (E_a = 0.59 eV) proceeds with CO_2 formation via C–H bond cleavage to generate IM10a. Notably, H_2 recombination from 2H species at the Co and N1 sites (IM11a) proceeds with an exceptionally low barrier of 0.30 eV, 37.5% lower than the vacuum-phase value of 0.48 eV, highlighting solvent stabilization of the transition state. Both CO_2 and H_2 exhibit weak physisorption on the catalyst surface, with desorption energies of merely 0.50 eV, ensuring rapid product release and active site regeneration. Structural alignment confirms that the $H_{N1}H_{N2}/CoCuN_6$-C catalyst fully recovers its initial configuration (IM5a), demonstrating robust recyclability for successive FA hydrogenation cycles without significant deactivation.

Moreover, the comparative analysis of transition states reveals a critical kinetic distinction: the TS8a state exhibits a 0.08 eV higher relative Gibbs free energy than TS9a (Figure S3), unambiguously identifying TS8a as the TDTS in the secondary FA decomposition pathway. This kinetic hierarchy is further amplified by thermodynamic perturbations in solvent compared to those in vacuum, the TDTS energy decreases by 0.20 eV while the TDI becomes destabilized (+0.13 eV) through weakened HCOOH adsorption (Figure S3). These concerted energetic shifts collectively reduce the overall activation barrier (δE) to 1.17 eV under explicit solvation conditions. Conclusively, our simulations using an explicit water model indicate that the decomposition of FA is kinetically more favorable on the hydrogenated NH-containing $CoCuN_6$-C catalyst ($H_{N1}H_{N2}/CoCuN_6$-C) compared to the pristine $CoCuN_6$-C catalyst. Additionally, the hydrogenated NH-containing $CoCuN_6$-C catalyst exhibits higher thermodynamic stability. These findings suggest

that the NH sites play a crucial role in FA decomposition, while the Co site, rather than the Cu site, is primarily responsible for the dehydrogenation of FA and H_2 formation.

2. Competing reaction pathway for CO byproduct using $CoCuN_6$-C

To elucidate the origin of reaction selectivity, we systematically compared the CO byproduct pathway with the dominant H_2/CO_2 production route using an explicit solvation model incorporating H_2O molecules. As illustrated in Figure S7 and Figure S8, the CO formation initiates from the IM5a intermediate on the $CoCuN_6$-C catalyst, where two *H species occupy bridge nitrogen sites. The formic acid molecule adsorbs at the Co site through coordination of its aldehyde oxygen (O2), positioning the C-H bond toward the N1 site. Subsequent C-H bond cleavage via nucleophilic attack by N1 transfers a hydrogen atom to this nitrogen center, forming a *COOH intermediate (IM7b) at the Co site. This rate-determining step exhibits a substantial activation barrier of 1.86 eV**,** attributed to the simultaneous rupture of the C-H bond and reorganization of the *COOH moiety. The pathway proceeds through C-O1 bond dissociation (barrier of +0.46 eV), yielding a chemisorbed CO molecule at the Co site ($d_{Co\text{-}C}$ = 1.87 Å) and a physisorbed H_2O molecule above the active center. Notably, CO desorption occurs spontaneously (desorption energy of −0.01 eV) due to weak adsorption strength. Crucially, the 1.86 eV activation barrier for CO formation substantially exceeds the 1.17 eV barrier of the main H_2/CO_2 production route, rationalizing the experimentally observed high selectivity for formic acid decomposition.[34] This mechanistic distinction originates from the more efficient *H–*H coupling dynamics in the main pathway versus the geometrically constrained *COOH intermediate stabilization required for CO generation.

3. FA decomposition using CoN_4-C as catalyst

In the absence of Cu doping, the CoN_4-C catalyst exhibits significantly reduced thermodynamic driving force for FA decomposition. As illustrated in Figure S9 and Figure S10, FA initially chemisorbs onto the Co site with an adsorption energy of –0.86 eV, followed by spontaneous dehydrogenation to yield a *HCOO intermediate through a barrierless, exothermic process. This sequence culminates in the formation of the thermally stable intermediate IM1c (TDI state). Subsequent N-H bond formation via solvent-derived hydrogen abstraction presents a substantial kinetic bottleneck, requiring an activation energy of 1.16 eV and reaction energy of 1.23 eV. The rate-determining step emerges as the *HCOO scission into CO_2 and surface-adsorbed *H species, which proceeds through the TS3c transition state with an energy barrier of 0.81 eV (TDTS state). These endergonic pathways correlate directly with the strong thermodynamic penalty for H_2 adsorption ($E_{ads}(H_2)$ = +1.81 eV, Figure 2), resulting in an overall reaction energy span (δE) of 2.04 eV. Strikingly, this δE value exceeds by 74% that observed for the hydrogenated $H_{N1}H_{N2}$/$CoCuN_6$-C catalyst (δE = 1.17 eV), demonstrating the critical role of Cu doping in modulating the catalyst's hydrogen affinity and orbital hybridization.

4. Comparison of FA decomposition barriers using different models

As summarized in Table S2, the CoN_4-C catalyst exhibits high activation energy barriers (δE) of 1.88 (vacuum) and 2.04 eV (explicit water model) for FA decomposition into H_2 and CO_2. In stark contrast, the $CoCuN_6$-C catalyst demonstrates significantly reduced δE values of 1.61 and 1.58 eV under vacuum and aqueous conditions, respectively, corresponding to energy barrier reductions of 0.27 and 0.46 eV. Notably, the competing pathway for CO byproduct formation is thermodynamically disfavored due to its prohibitively high barrier (1.86 eV) in the solvent model.

This enhanced catalytic performance of $CoCuN_6$-C stems from the weakened *H adsorption at hydrogenated NH moieties ($H_{N1}H_{N2}$/$CoCuN_6$-C) compared to the pristine N sites. The reduced *H binding energy (0.51 eV vs. –0.38 eV for pristine sites) directly correlates with the lowered dehydrogenation barriers. These results underscore the crucial role of electronic modulation in nitrogen atoms via dual-metal synergy (M1-N-M2): the *d*-orbital hybridization between Co and Cu alters the ligand field symmetry, shifting the N *p*-band center upward and enhancing charge transfer to adsorbed intermediates. Crucially, this study reveals that heteroatomic N sites, traditionally viewed as structural stabilizers, can be dynamically engineered as catalytic hotspots for dehydrogenation, challenging the conventional paradigm of metal-centric active sites. The findings establish a dual-functional mechanism where the M1-N-M2 moiety optimizes *H desorption kinetics, offering a generalizable strategy for designing multifunctional DACs in hydrogenation catalysis.

References:

S1. Chakrapani, K.; Bendt, G.; Hajiyani, H.; Lunkenbein, T.; Greiner, M. T.; Masliuk, L.; Salamon, S.; Landers, J.; Schlögl, R.; Wende, H.; Pentcheva, R.; Schulz, S.; Behrens, M. The Role of Composition of Uniform and Highly Dispersed Cobalt Vanadium Iron Spinel Nanocrystals for Oxygen Electrocatalysis. *ACS Catal.* **2018**, *8*, 1259-1267.

S2. Galiaei, E. M. Photocatalytic Efficiency for CO_2 Reduction of Co and Cluster Co_2O_2 Supported on g-C_3N_4: A Density Functional Theory and Machine Learning Study. *Langmuir*, **2024**, *40*, 7871-7882.

Table S2. Bond length (unit: Å) for several bonds in $CoCuN_6$-C, $H_{N1}H_{N2}$/$CoCuN_6$-C, $H_{N2}H_{Co}$/$CoCuN_6$-C, and 4H/$CoCuN_6$-C structures

Bond	$CoCuN_6$-C	$H_{N1}H_{N2}$/$CoCuN_6$-C	$H_{N2}H_{Co}$/$CoCuN_6$-C	4H/$CoCuN_6$-C
Co-Cu	2.61	2.57	2.58	2.64
Co-N1	1.86	1.90	1.83	2.06
Co-N2	1.86	1.90	1.94	1.86
Co-N3	1.90	1.92	1.88	1.94
Co-N4	1.90	1.92	1.93	1.91
Cu-N1	1.89	2.20	1.86	2.61
Cu-N2	1.89	2.20	2.06	2.04
Cu-N5	1.92	2.04	1.91	2.04
Cu-N6	1.92	2.05	1.97	2.03
N1-H1	/	1.02	/	1.03
N2-H2	/	1.02	1.03	1.03
Co-H1	/	/	1.43	/
Co-H4	/	/	/	1.45
N1-H3	/	/	/	1.03

Table S3. Energy barriers (δE) for the formation of H_2 pathway and CO side pathway using $CoCuN_6$-C, $H_{N1}H_{N2}/CoCuN_6$-C, and CoN_4-C

	$CoCuN_6$-C	$H_{N1}H_{N2}/CoCuN_6$-C	CoN_4-C
Vacuum	1.61	1.50	1.88
Solvent	1.58	1.17	2.04
Solvent (CO)	/	1.86	/

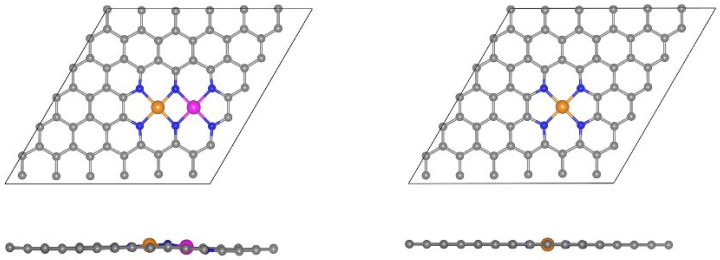

(a) $CoCuN_6$-C (b) CoN_4-C

Figure S1. Optimized structures of (a) dual-atoms catalyst $CoCuN_6$-C and (b) single-atom catalyst CoN_4-C.

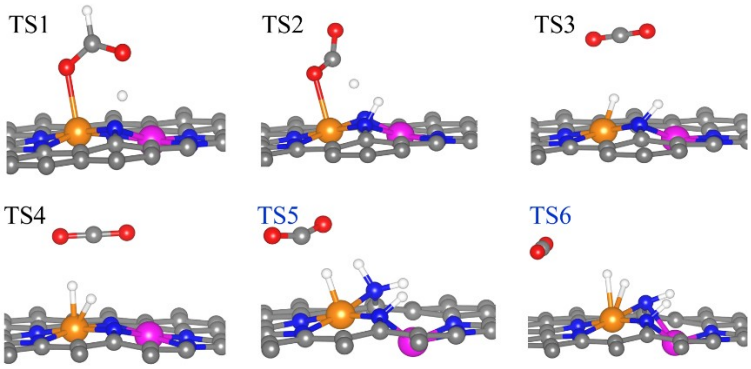

Figure S2. Structures of the transition states for HCOOH decomposition into CO_2 and H_2 on $CoCuN_6$-C catalyst in vacuum (supplementary to Figure 5).

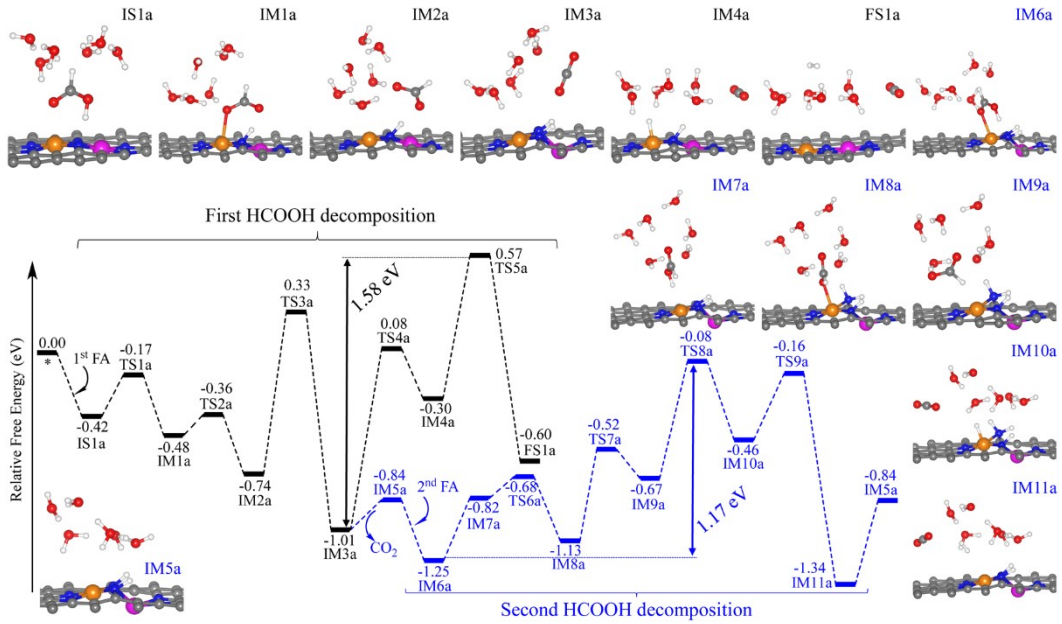

Figure S3. Reaction profiles for HCOOH decomposition into CO_2 and H_2 using $CoCuN_6$-C catalyst with explicit water model.

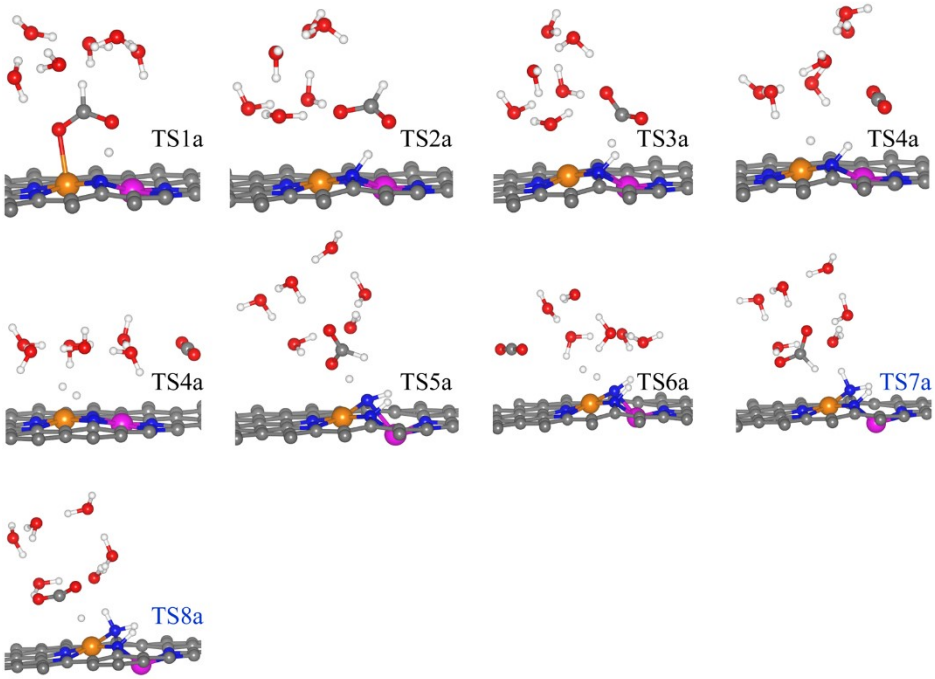

Figure S4. Structures of the transition states for HCOOH decomposition into CO_2 and H_2 on $CoCuN_6$-C catalyst with explicit water model (supplementary to Figure S3).

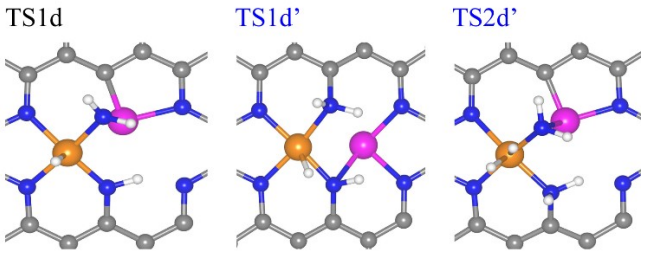

Figure S5. Structures of the transition states for the over-hydrogenation of NH_2 site in 4H/$CoCuN_6$-C structure (supplementary to Figure 6).

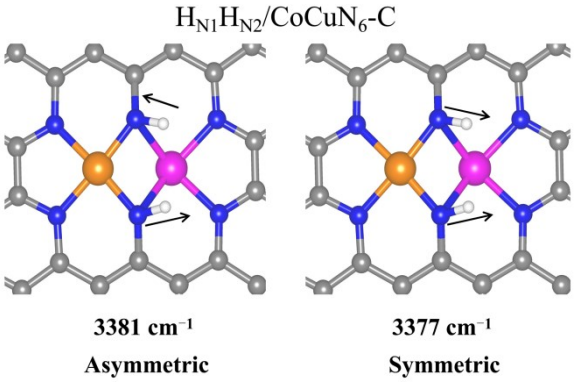

Figure S6. Vibration modes for N-H bonds in $H_{N1}H_{N2}/CoCuN_6$-C structure.

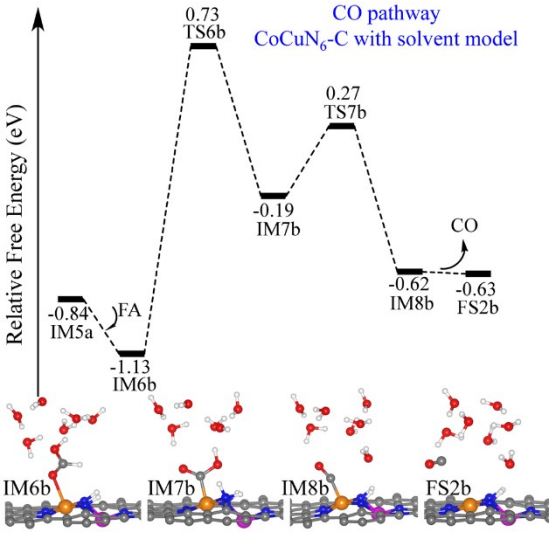

Figure S7. Reaction profiles for HCOOH decomposition into CO byproduct using $CoCuN_6$-C catalyst with explicit water model.

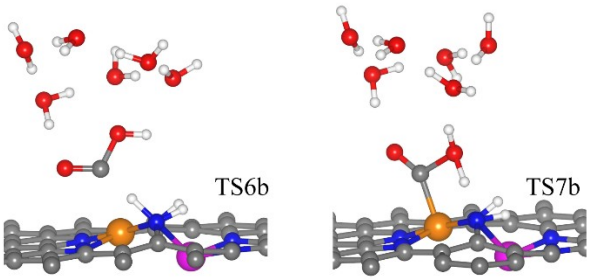

Figure S8. Structures of the transition states for HCOOH decomposition into CO and H_2O on $CoCuN_6$-C catalyst with explicit water model (supplementary to Figure S7).

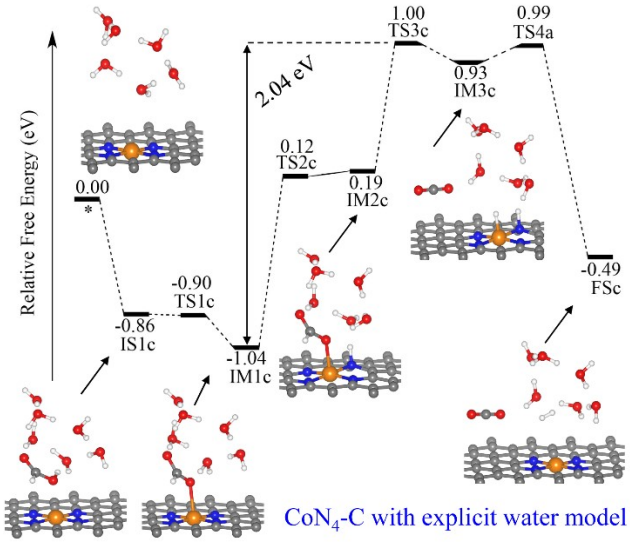

Figure S9. FA decomposition pathways using CoN_4-C as catalyst under explicit water model.

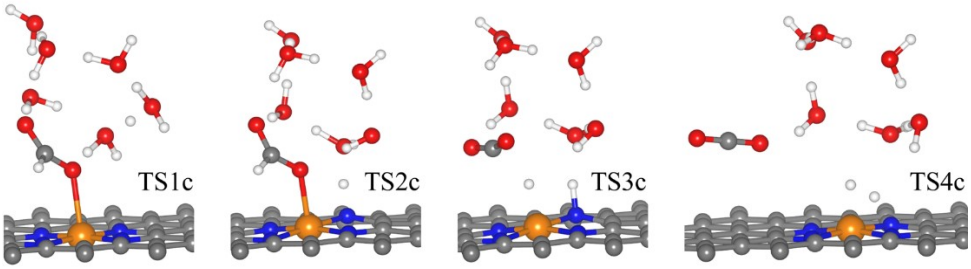

Figure S10. Structures of the transition states for HCOOH decomposition into H_2 and CO_2 on CoN_4-C catalyst with explicit water model (supplementary to Figure S9).